# Mineral chemistry of Mahadevpur H4/5 chondrite: characterization of nanodiamonds through micro-Raman spectroscopic studies

**Bhaskar J. Saikia[1,*], G. Parthasarathy[2], N. V. Chalapathi Rao[3,4], Vikas Seth[3] and Rashmi R. Borah[5]**

[1]Department of Physics, Anandaram Dhekial Phookan College, Nagaon 782 002, India
[2]School of Natural and Engineering Sciences, National Institute of Advanced Studies, Indian Institute of Science Campus, Bengaluru 560 012, India
[3]Centre of Advanced Study in Geology, Institute of Science, Banaras Hindu University, Varanasi 221 005, India
[4]National Centre for Earth Science Studies, Thiruvananthapuram 695 011, India
[5]Department of Physics, Nagaon University, Nagaon 782 001, India

**Here, we present comprehensive electron probe micro analysis, laser Raman spectroscopic and X-ray diffraction (XRD) studies on the Mahadevpur H4/5 chondrite. The calculated full width at half maximum (FWHM) value of ~14–17 cm$^{-1}$ for the Raman peaks in the Mahadevpur meteorite is in accordance with the shock stage of S4 with medium shock pressure regime of 30–35 GPa. The nanodiamonds were characterized with the observation of Raman peaks at 1333–1358 cm$^{-1}$ and 1600 cm$^{-1}$. The FWHM value of the Raman peaks reflects shock metamorphism in the meteorite. The XRD technique provides further independent validation of the nanodiamonds.**

**Keywords:** Chondrite, mineral chemistry, nanodiamonds, shock metamorphism, spectroscopic analysis.

THE composition of chondrites is primarily ultramafic, made up of iron, magnesium, silicon and oxygen. Chondrites comprise four main parts: fine-grained matrix material, chondrules, Fe–Ni metal and refractory inclusions such as amoeboid olivine aggregates and Ca–Al-rich inclusions. In the solar nebula, Fe–Ni-metal is produced by high-temperature processes like evaporation and condensation[1]. Chondrites are known to be meteorites that hold maximum information about the formation of the solar system. Their components formed during the formation of the solar system, approximately 4,567 million years ago, making them the oldest known rocks. Additionally, the abundance of non-volatile elements in these rocks is comparable to that of the solar photosphere. Metallic Fe–Ni grains can be found both inside and outside the chondrules. They are up to a millimetre in size and were formed at high temperatures, just like chondrules and refractory inclusions. Chondrites are primarily composed of igneous particles called chondrules, which crystallized rapidly within minutes to hours. They are 0.01–10 mm in size, mostly made of olivine and pyroxene, and frequently contain metallic Fe and Ni. Due to partial melting or the accumulation of other particles during the solidification process, many chondrules have irregular shapes, although some are rounded because they were once completely molten. Understanding the chemical composition and mineral chemistry of meteorites is essential for comprehending the history and dynamics of the solar system[2–13].

The Mahadevpur H4/5 chondrite was a multiple fall observed on 21 February 2007 at Mahadevpur (lat. 27°40′N, long. 95°47′E), near Namsai town, Arunachal Pradesh (and adjoining areas), North East India at 09:10 IST (ref. 14). The total known weight of the Mahadevpur chondrite is 70.5 kg (refs 14, 15). At present, only two ordinary chondrites of type H4/5 are found in India. The first meteorite belonging to this type was found in Kendrapara, Odisha (2003) and the second in Mahadevpur (2007)[14,16]. The infrared spectroscopic analyses of the Mahadevpur chondrite in previous studies suggested that it has partially disordered or glassy silicates structure[17–19]. Dehingia and Baruah[20] reported the red luminescence of olivine in the Mahadevpur meteorite using laser-induced fluorescence. The lack of compositional variation in the olivine found in the chondrules and matrix indicates that the Mahadevpur is an equilibrated H-chondrite. The noble gas analyses indicate the cosmic-ray exposure age of the meteorite as 6 Ma (ref. 21). Diamonds have been found in many meteorites (e.g. Allende, Murchison, Canyon Diablo and Novo Urei), interplanetary dust particles and comet dust[22]. Presolar diamonds, which have a diameter of a few nanometres and were formed prior to the formation of our solar system, can be found in the most primitive matter, such as carbonaceous chondrites[23]. Nanodiamonds are widely distributed in the interstellar medium; diamonds of size >50 nm have been identified in HD 97048 and Elias 1 Herbig Ae/Be stars[24]. In this study, we report the mineral chemistry and presence of nanodiamonds as well as shock metamorphic features in the Mahadevpur meteorite using laser Raman spectroscopy, supported by data obtained from scanning electron microscopy (SEM), electron probe micro analysis (EPMA) and X-ray diffraction (XRD) analysis.

*For correspondence. (e-mail: vaskaradp@gmail.com)

## Experimental techniques

The studied specimen from Mahadevpur was hard, light grey in colour, sub-angular and coarse-grained having high specific gravity (~3.42 g/cm$^3$), which when cut revealed a shining appearance. The hand specimen, when brought near a magnet indicated a high ferromagnetic component. A polished thin section was prepared and studied under transmitted light using a microscope (Olympus BX51, Japan). The same thin section was subsequently coated with a ~50 nm carbon layer (using LEICA-EM ACE200 instrument, Germany) for probe analysis. Back-scattered electron (BSE) imaging as well as mineral chemistry analysis were carried out using SEM (EV018) and EPMA (Camera SX5) respectively, at the Department of Geology, Banaras Hindu University (BHU), Varanasi. The EPMA instrument operated at a voltage of 15 kV and a current of 10 nm, utilizing the $LaB_6$ source for electron beam generation in the electron gun. Andradite served as the internal standard to validate the positions of crystals such as SP1-TAP, SP2-LiF, SP3-LPET, SP4-LTAP and SP5-PET. For the analyses X-ray lines, including F-K$\alpha$, Na-K$\alpha$, Mg-K$\alpha$, Al-K$\alpha$, Si-K$\alpha$, P-K$\alpha$, Cl-K$\alpha$, K-K$\alpha$, Ca-K$\alpha$, Ti-K$\alpha$, Cr-K$\alpha$, Mn-K$\alpha$, Ni-K$\alpha$ and Fe-K$\alpha$ were used. Respective standards such as fluorite, albite, peridot, corundum, orthoclase, apatite, NaCl, orthoclase, wollastonite, rutile, chromite, rhodonite, nickel metal and hematite (CAMECA-AMETEK, France), were used for routine calibration to quantify the results. Regular quality checks with standards confirmed that the analysis precision was continuously better than 1% for major elements and 5% for trace elements. The Raman spectra were collected on the bulk meteorite sample using a Nd : YAG laser with a power of ~5 mW, that used an excitation source having wavelength 532 nm combined with a micro-Raman spectrometer (Jobin Yvon Horiba LabRam-HR) equipped with an Olympus microscope having 10X, 50X and 100X objectives. This set-up uses 1800 grooves/mm grating in the range 100–3000 cm$^{-1}$ and includes a motorized $x$–$y$ stage. Calibration was performed using a silicon wafer ($520.7 \pm 0.5$ cm$^{-1}$). The technique of identifying minerals based on their spectral signatures is relatively simple due to excellent peak position accuracy ($\pm 0.5$ cm$^{-1}$) and precision ($\pm 0.1$ cm$^{-1}$) of the instrument over the entire Raman spectral range. The precise Stokes lines were measured using an edge filter. A Gaussian fit was used for data interpretation to pinpoint the precise location of each peak maximum. Minerals were identified by comparing the band positions in the spectra with the Raman data on the end-member minerals at room temperature and pressure (RRUFF-database http://rruff.info/). At room temperature (28°C), Raman data were obtained between wavenumbers 100 and 2000 cm$^{-1}$. Ranges of counting times, from 10 to 60 sec, were used to collect the spectra. A portion of the powered sample was used for XRD analysis employing a diffractometer (Philips PW 3710/31, Philips, USA), scintillation counter, and CuK$\alpha$ radiation ($\lambda = 1.54184$) with a Ni filter operating at 40 kV and 35 mA. The data were collected using step scans at room temperature within the $2\theta$ range of 10°–80°. The step width and counting time were set at 0.02° and 5 sec respectively. The divergence and receiving slits were measured at 0.5 and 0.3 mm respectively. The typical room temperature data released for individual minerals allowed for the identification of the individual mineral phases (RRUFF-database http://rruff.info/).

## Results and discussion

The petrography revealed a coarse to medium crystalline chondritic texture displaying a diverse array of chondrules such as barred olivine, porphyritic olivine-pyroxene, granular olivine-pyroxene and cryptocrystalline chrondules dispersed in a relatively medium to fine crystalline matrix (Figure 1). The chondrules have apparent sizes between 0.2 and 1.2 mm. The Mahdevapur meterorite constituted dominantly comprises olivine, low Ca-pyroxene, and opaques (Fe–Ni phases) around ~25%, and minor other accessory minerals like chlor-apatite, merrillite and plagioclase feldspar. The same uniform grey scale in BSE images represents similarity in composition of chondules and the matrix. A significant portion of the chondrules is composed of olivine or pyroxene phenocrysts. The chondrules are mostly devoid of metal and sulphide, although these components could be found in the matrix as irregular grains or as small pockets. Olivine grains occur both as chondrules and in the matrix and could be easily distinguished by their high relief, lack of cleavage, granular morphology and high second-order interference colours. Pyroxene also occur as chondrules, but are relatively smaller in size than that of the olivine; a few pyroxene grains display elongated as well as radiated nature. Low-calcium pyroxene can be identified easily in crossed polarized light by low first-order interference colour. Olivine and pyroxene show minor mottled extinction. Native Fe, larger kamacite, taenite, troilite nodules and minor chromite are irregular in shape and have a non-uniform distribution. From their morphology and mode of occurrence, it could be inferred that they occurred mainly as epigenetic melt pockets surrounding the primary phases. The thin section lacked volatile phases, and was fresh and unaltered, except for some surficial rust staining.

The olivine present in the chondrules and the matrix is the same and of Mg-rich variety. The olivine compositionally ranged from $Fo_{79.9}Fa_{10.9}Te_{0.4}$ to $Fo_{88.4}Fa_{19.6}Te_{0.9}$ (Table 1; Fo: forsterite, Fa: fayalite, and Te: tephroite). The Mg/Fe ratios remain almost constant; no typical chemical zoning is observed, representing equilibrium conditions. The pyroxenes were mainly clinoenstatites, with a few augite and diopside compositions (Table 2). The recalculated pyroxene compositions are shown in the Wo–En–Fs diagram (Figure 2). The Mg# ranged from ~0.85 to 0.90. Enstatite is often associated with forsterite. All these

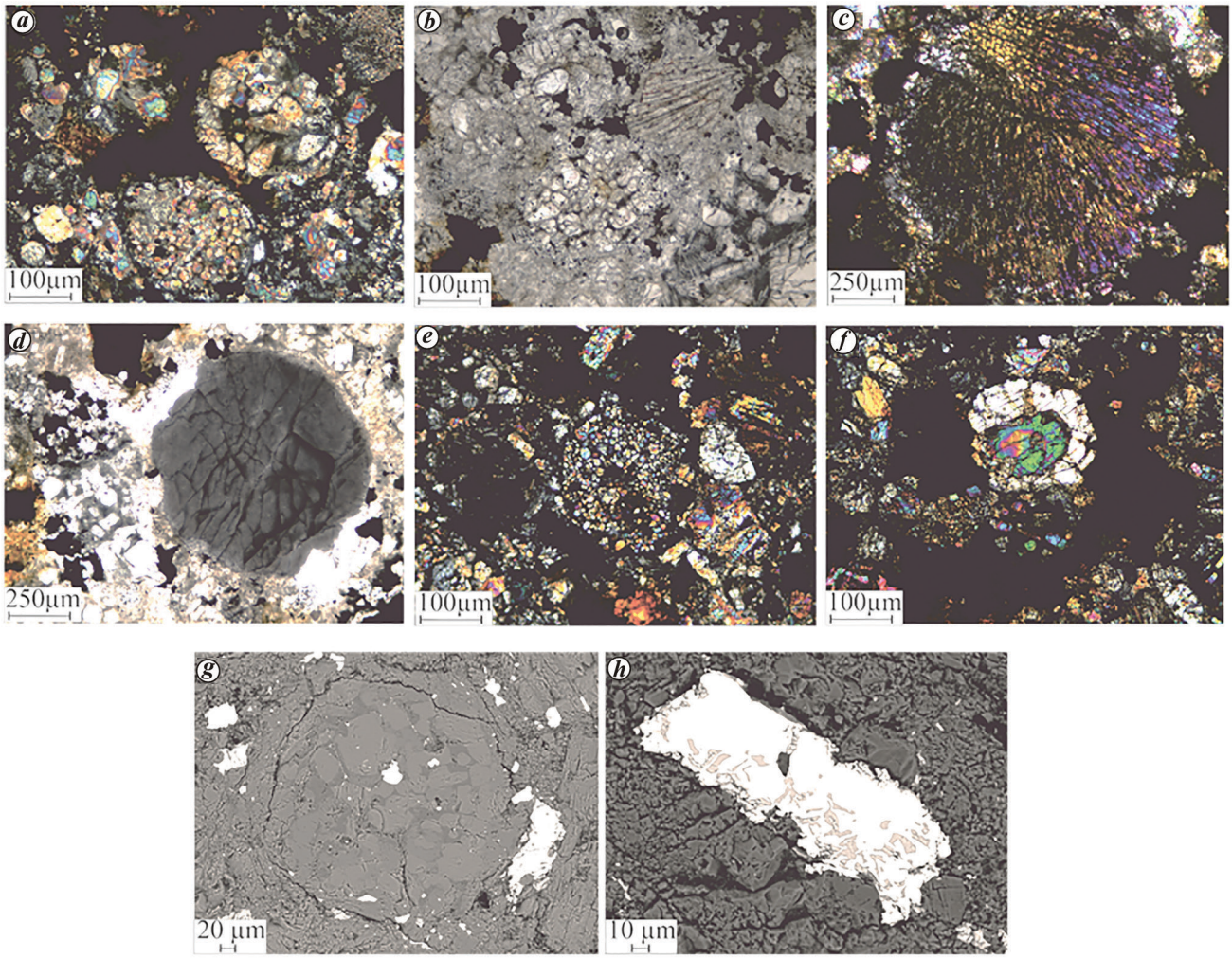


**Figure 1.** Photomicrographs of the Mahadevpur meteorite. ***a***, Prominent olivine chrondule surrounded by Fe–Ni phases in crossed polarized light (XPL). Mean diameter of the chondrules is ~0.3 mm. ***b***, A relatively chondrule-free portion showing slightly transparent cloudy matrix in PPL. In the upper right portion, elongated radiating crystal of low-calcium pyroxene (LCP) is present. ***c***, Barred olivine chondrule with olivine dendrite crystals growing inwards from a molten droplet leaving behind the mesostasis portion. ***d***, A nearly spherical mass of cryptocrystalline enstatite. ***e***, Granular olivine chondrule. ***f***, Olivine rimmed by enstatite crystal. ***g***, A well-developed enstatite chondrule in backscattered electron (BSE), the interstitial mass as a relatively darker portion is feldspathic in composition. ***h***, Exsolution feature of troilite and taenite in BSE.

pyroxenes were well equilibrated, except for those which were smaller and poorly crystallized. However, three metallic phases were dominant in the Mahadevpur meteorite (Table 3), ranging from kamacite (near pure end Fe)-taenite $\gamma$-(Fe, Ni), and tetrataenite (Fe–Ni). These phases formed a solid solution between Fe (+Co) $\leftrightarrow$ Ni (+Cu). In the Mahadevpur meteorite, the complete exsolved phases are rarely seen, representing under-cooling from a quenched melt (Figure 3). Another abundant phase in meteorite was the iron sulphide phase (troilite). It is either associated with taenite or formed randomly dispersed grains. The average ($n$ = 28) composition of the analysed troilite contains (in wt%) is Fe: 60.736, Zn: 0.039, Ni: 6.575, Co: 0.017, S: 31.835, Ag: 0.004, Au: 0.003, Cu: 0.106, Pb: 0.175, Se: 0.019 and As: 0.038 (Table 4). From the mineral chemistry of ferro-magnesium and Fe alloy minerals analysed, it can be seen that most of Ni is restricted to Fe alloy phases and does not partition into any Fe–Mg minerals which forms the bulk of the Mahadevpur meteorite. In addition, the presence of native iron and troilite indicates that a highly reducing environment existed during crystallization of this meteorite. Chromite grains occur as inclusions in the metals, in addition to these minerals. SEM-EDS analysis revealed several other phases like pure chromite, chlorapatite, merrillite and plagioclase feldspar. These minerals were either too fine or lacked a distinct morphology, and occupied interstitial position. EDS spectra of the accessory phases obtained by SEM are not shown here.

The Raman spectral region 100–1200 $cm^{-1}$ revealed five characteristic bands for olivine at 826–819 $cm^{-1}$

**Table 1.** Some representative analyses (oxide wt %) of olivine from the Mahadevpur meteorite in this study

| | Fo 1 | Fo 2 | Fo 3 | Fo 4 | Fo 5 | Fo 6 | Fo 7 | Fo 8 | Fo 9 | Fo 10 |
|---|---|---|---|---|---|---|---|---|---|---|
| $SiO_2$ | 37.557 | 38.252 | 38.445 | 37.333 | 38.043 | 38.269 | 38.642 | 38.026 | 38.232 | 37.688 |
| $TiO_2$ | 0.185 | 0.002 | 0.028 | 0.03 | 0.026 | 0.014 | 0.036 | 0.039 | 0.034 | 0 |
| $Al_2O_3$ | 0.009 | 0 | 0.251 | 0 | 0 | 0 | 0 | 0 | 0.058 | 0 |
| $Cr_2O_3$ | 0.084 | 0 | 0 | 0.099 | 0.015 | 0.002 | 0.058 | 0.03 | 0.115 | 0 |
| FeO | 18.132 | 17.83 | 17.1 | 17.667 | 16.91 | 17.852 | 17.041 | 17.288 | 16.236 | 17.775 |
| MnO | 0.469 | 0.482 | 0.612 | 0.522 | 0.511 | 0.435 | 0.55 | 0.538 | 0.551 | 0.563 |
| MgO | 42.937 | 43.123 | 43.026 | 42.523 | 43.047 | 42.931 | 43.275 | 43.119 | 42.889 | 42.671 |
| CaO | 0.073 | 0.038 | 0.112 | 0.059 | 0.051 | 0.1 | 0.042 | 0.087 | 0.113 | 0.052 |
| Sum | 99.446 | 99.727 | 99.574 | 98.233 | 98.602 | 99.602 | 99.643 | 99.127 | 98.228 | 98.749 |
| Formula on the basis of four oxygen | | | | | | | | | | |
| Si | 0.96 | 0.973 | 0.979 | 0.965 | 0.976 | 0.976 | 0.983 | 0.972 | 0.984 | 0.969 |
| Ti | 0.004 | 0 | 0.001 | 0.001 | 0 | 0 | 0.001 | 0.001 | 0.001 | 0 |
| Al | 0 | 0 | 0.008 | 0 | 0 | 0 | 0 | 0 | 0.002 | 0 |
| Cr | 0.002 | 0 | 0 | 0.002 | 0 | 0 | 0.001 | 0.001 | 0.002 | 0 |
| $Fe^{3+}$ | 0.072 | 0.053 | 0.034 | 0.068 | 0.046 | 0.048 | 0.032 | 0.054 | 0.026 | 0.062 |
| $Fe^{2+}$ | 0.316 | 0.326 | 0.33 | 0.314 | 0.317 | 0.332 | 0.33 | 0.316 | 0.324 | 0.32 |
| Mn | 0.01 | 0.01 | 0.013 | 0.011 | 0.011 | 0.009 | 0.012 | 0.012 | 0.012 | 0.012 |
| Mg | 1.635 | 1.636 | 1.633 | 1.638 | 1.647 | 1.631 | 1.64 | 1.643 | 1.646 | 1.635 |
| Ca | 0.002 | 0.001 | 0.003 | 0.002 | 0.001 | 0.003 | 0.001 | 0.002 | 0.003 | 0.001 |
| Mg/Fe | 5.182 | 5.015 | 4.946 | 5.213 | 5.192 | 4.911 | 4.972 | 5.205 | 5.085 | 5.112 |
| Te | 0.517 | 0.527 | 0.668 | 0.582 | 0.562 | 0.476 | 0.598 | 0.591 | 0.606 | 0.623 |
| Fa | 16.092 | 16.537 | 16.705 | 16.002 | 16.06 | 16.838 | 16.644 | 16.02 | 16.334 | 16.258 |
| Fo | 83.391 | 82.936 | 82.627 | 83.416 | 83.378 | 82.686 | 82.758 | 83.389 | 83.06 | 83.119 |

**Table 2.** Some representative analyses (oxide wt %) of pyroxene from the Mahadevpur meteorite

| | En 1 | En 2 | En 3 | En 4 | En 5 | En 6 | Di 1 | Di 2 | Aug-01 | Aug-02 |
|---|---|---|---|---|---|---|---|---|---|---|
| $SiO_2$ | 56.845 | 52.923 | 56.11 | 55.766 | 55.671 | 56.197 | 50.23 | 50.509 | 53.674 | 56.612 |
| $TiO_2$ | 0.123 | 0.107 | 0.11 | 0.181 | 0.146 | 0.113 | 0.766 | 0.659 | 0.281 | 0.271 |
| $Al_2O_3$ | 0.233 | 3.156 | 0.304 | 0.289 | 0.272 | 0.088 | 1.127 | 1.062 | 1.363 | 3.66 |
| $Cr_2O_3$ | 0.159 | 0.173 | 0.533 | 0.159 | 0.216 | 0 | 1.053 | 0.855 | 1.059 | 0.672 |
| FeO | 10.553 | 10.528 | 11.303 | 10.371 | 10.898 | 10.626 | 5.11 | 3.74 | 7.179 | 2.586 |
| MnO | 0.578 | 0.694 | 0.54 | 0.605 | 0.706 | 0.707 | 0.532 | 0.262 | 0.427 | 0.325 |
| MgO | 31.251 | 30.126 | 31.298 | 30.415 | 30.681 | 30.981 | 20.798 | 19.751 | 23.277 | 13.986 |
| CaO | 0.628 | 0.715 | 0.526 | 1.14 | 1.01 | 0.595 | 21.295 | 21.03 | 12.165 | 20.034 |
| $Na_2O$ | 0.029 | 0.074 | 0.053 | 0.048 | 0.027 | 0.026 | 0.59 | 0.599 | 0.408 | 1.802 |
| $K_2O$ | 0.002 | 0.034 | 0.048 | 0.014 | 0.023 | 0.009 | 0.016 | 0.042 | 0.016 | 0.152 |
| Sum | 100.401 | 98.529 | 100.824 | 98.987 | 99.651 | 99.342 | 101.517 | 98.509 | 99.849 | 100.1 |
| Formula on the basis of six oxygen | | | | | | | | | | |
| Si | 1.995 | 1.888 | 1.964 | 1.988 | 1.973 | 1.994 | 1.783 | 1.846 | 1.93 | 2.057 |
| Ti | 0.003 | 0.003 | 0.003 | 0.005 | 0.004 | 0.003 | 0.02 | 0.018 | 0.008 | 0.007 |
| Al | 0.01 | 0.133 | 0.013 | 0.012 | 0.011 | 0.004 | 0.047 | 0.046 | 0.058 | 0.157 |
| Cr | 0.004 | 0.005 | 0.015 | 0.004 | 0.006 | 0 | 0.03 | 0.025 | 0.03 | 0.019 |
| $Fe^{2+}$ | 0.31 | 0.314 | 0.331 | 0.309 | 0.323 | 0.315 | 0.152 | 0.114 | 0.216 | 0.079 |
| Mn | 0.017 | 0.021 | 0.016 | 0.018 | 0.021 | 0.021 | 0.016 | 0.008 | 0.013 | 0.01 |
| Mg | 1.635 | 1.602 | 1.633 | 1.616 | 1.621 | 1.638 | 1.101 | 1.076 | 1.248 | 0.758 |
| Ca | 0.024 | 0.027 | 0.02 | 0.044 | 0.038 | 0.023 | 0.81 | 0.823 | 0.469 | 0.78 |
| Na | 0.002 | 0.005 | 0.004 | 0.003 | 0.002 | 0.002 | 0.041 | 0.042 | 0.028 | 0.127 |
| K | 0 | 0.002 | 0.002 | 0.001 | 0.001 | 0 | 0.001 | 0.002 | 0.001 | 0.007 |
| Mg# | 0.841 | 0.836 | 0.832 | 0.839 | 0.834 | 0.839 | 0.879 | 0.904 | 0.853 | 0.906 |
| Wo | 1.189 | 1.392 | 0.987 | 2.19 | 1.916 | 1.132 | 39.053 | 40.771 | 24.106 | 47.927 |
| En | 82.339 | 81.651 | 81.72 | 81.338 | 80.943 | 82.03 | 53.079 | 53.285 | 64.183 | 46.561 |
| Fs | 16.472 | 16.957 | 17.293 | 16.472 | 17.141 | 16.837 | 7.868 | 5.945 | 11.711 | 5.512 |

(band 1), 858–849 $cm^{-1}$ (band 2), 883–881 $cm^{-1}$ (band 3), 920–914 $cm^{-1}$ (band 4) and 967–951 $cm^{-1}$ (band 5). Band 1, band 2 and band 5 were attributed to the $A_g$ symmetry, band 3 to the $B_{2g}$ symmetry, and band 4 to the $B_{3g}$ symmetry. The observed Raman peaks at 822, 854, 916 and 952 $cm^{-1}$ in the spectrum were characteristic of forsterite (Figure 4). The observed doublet at 822 and 854 $cm^{-1}$ in the spectrum as a result of the coupling between the symmetric ($\nu 1$) and anti-symmetric ($\nu 3$) stretching modes of Si–$O_{nb}$ bonds in the $SiO_4$ tetrahedra[9,10,17,25,26]. However,

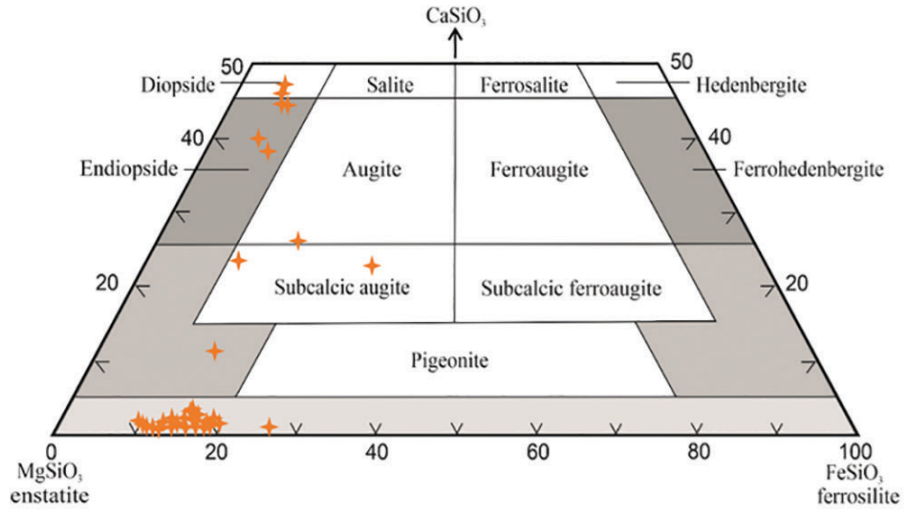


**Figure 2.** Wo–En–Fs ternary diagram of pyroxenes from the present study.

**Table 3.** Some representative analyses (wt %) of metals from the Mahadevpur meteorite

| | Ka 1 | Ka 2 | Ka 3 | Tae 1 | Tae 2 | Tae 3 | Tae 4 | Tae 5 | Tae 6 |
|---|---|---|---|---|---|---|---|---|---|
| Fe | 92.628 | 94.092 | 93.181 | 66.862 | 72.581 | 63.401 | 46.402 | 51.439 | 52.454 |
| Zn | 0 | 0.113 | 0 | 0.127 | 0 | 0 | 0.305 | 0.009 | 0 |
| Ni | 4.728 | 4.669 | 6.624 | 32.834 | 24.949 | 34.895 | 49.994 | 47.464 | 47.37 |
| Co | 0.776 | 0.541 | 0.576 | 0 | 0.218 | 0.213 | 0.084 | 0.108 | 0.148 |
| S | 0.009 | 0 | 0.002 | 0.03 | 0 | 0.004 | 3.037 | 0.002 | 0.007 |
| Ag | 0 | 0 | 0 | 0.084 | 0.029 | 0 | 0 | 0 | 0 |
| Au | 0 | 0 | 0 | 0 | 0 | 0 | 0 | 0 | 0 |
| Cu | 0.358 | 0.17 | 0.209 | 0.194 | 0.216 | 0.484 | 0.551 | 0.687 | 0.572 |
| Pb | 0.253 | 0.153 | 0.126 | 0.005 | 0.151 | 0.074 | 0.14 | 0.233 | 0.238 |
| Se | 0 | 0.041 | 0 | 0 | 0 | 0 | 0.024 | 0 | 0.049 |
| As | 0.033 | 0.059 | 0.078 | 0.037 | 0.049 | 0.058 | 0 | 0.031 | 0.031 |
| Sum | 98.785 | 99.84 | 100.796 | 100.173 | 98.194 | 99.128 | 100.539 | 99.972 | 100.869 |

the peak positions varied with the compositional ratio of fayalite (Fa) to forsterite (Fo), and the relative height of this doublet was dependent on the crystal orientation. Additionally, at 879 $cm^{-1}$, close to the recognizable olivine doublets, the Raman spectrum showed some ringwoodite signals[27].

The Raman spectrum of the Mahadevpur meteorite show distinctive peaks at 1008, 683, 663 and 340 $cm^{-1}$ in the characteristic regions (~1000, ~670 and 400–200 $cm^{-1}$) of pyroxene (Figure 5). Generally, the Mg/Fe and Wo contents in pyroxene causes a gradual shift in the Raman peak frequencies in these regions. The most intense Raman bands at 1008, 683 and 663 $cm^{-1}$ were attributed to the stretching $\nu$(Si–$O_{nb}$) and $\nu$(Si–$O_b$–Si) respectively, in which $O_{nb}$ and $O_b$ represent non-bonded oxygen and chain-bonded oxygen of the $SiO_4$ tetrahedron corresponding to the two oxygen-shared $SiO_4$ tetrahedra of inosilicates[9–12,28]. The peaks at 403, 413, 510, 542, 580, 605, 663 and 683 $cm^{-1}$ resulted from the Si and Mg displacements as well as internal bending of the $SiO_4$ tetrahedron ($\nu$2 and $\nu$4). However, traces of maskelynite could be identified from the peaks at 510 and 580 $cm^{-1}$ (ref. 29). The lattice modes, which included the rotations and translations of $SiO_4$ units and the translations of octahedral cations ($Mg^{2+}$, $Fe^{2+}$) in the crystal lattice[28], were primarily responsible for the Raman peaks below the 400 $cm^{-1}$ region, viz. at 236, 298 and 340 $cm^{-1}$. The cage-shear modes yielded Raman peaks at 189 and 131 $cm^{-1}$. These peaks offer significant insights into temperature dependence, even though their low intensities are caused by the polarizabilities of the octahedral structural units[28,30,31].

The calculated full width at half maximum (FWHM) value for the forsterite peaks in the Mahadevpur sample was about 14 $cm^{-1}$ for the component at 822 and 17 $cm^{-1}$ for the component at 854 $cm^{-1}$. However, the well-crystallized terrestrial olivines showed FWHM of 9.5 $cm^{-1}$ for the band at ~820 and 10.5 $cm^{-1}$ for the band at ~854 $cm^{-1}$ (ref. 32). The computed FWHM values were greater than those found in terrestrial olivines with well-crystallized crystals, which indicates a certain structural disorder in the meteorite sample. This degree of crystal structural disorder is from shock deformation[33], and spans FWHM

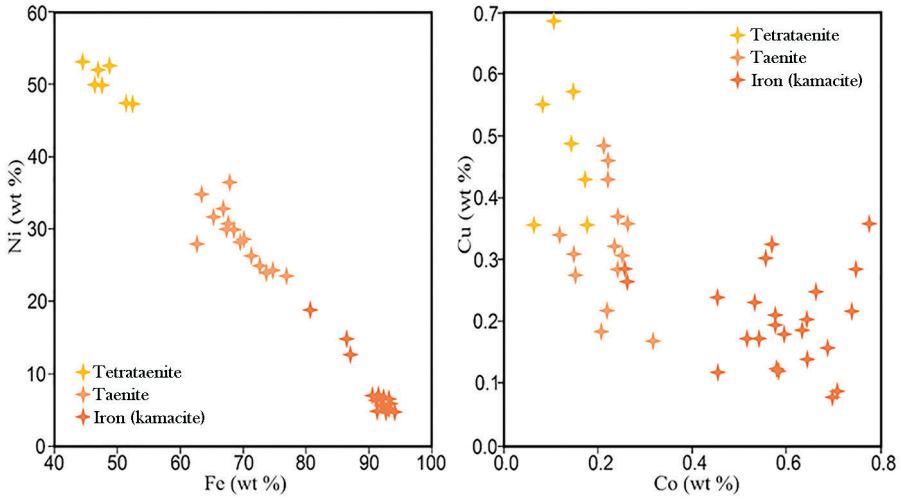


**Figure 3.** Atomic substitution diagram for Fe–Ni phases: Ni versus Fe (wt%) and Cu versus Co (wt%).

**Table 4.** Some representative analyses (wt%) of troilite from the Mahadevpur meteorite

| | Tro 1 | Tro 2 | Tro 3 | Tro 4 | Tro 5 | Tro 6 | Tro 7 | Tro 8 | Tro 9 | Tro 10 |
|---|---|---|---|---|---|---|---|---|---|---|
| Fe | 62.397 | 62.252 | 62.189 | 61.731 | 62.374 | 61.777 | 61.254 | 62.319 | 62.492 | 61.775 |
| Zn | 0 | 0 | 0 | 0 | 0 | 0 | 0 | 0 | 0 | 0 |
| Ni | 0.057 | 0 | 0 | 0.032 | 0 | 0 | 0 | 0 | 0 | 0 |
| Co | 0 | 0 | 0 | 0 | 0 | 0 | 0 | 0.021 | 0 | 0.021 |
| S | 37.182 | 36.577 | 36.793 | 36.76 | 36.433 | 36.807 | 35.787 | 36.177 | 37.132 | 35.928 |
| Ag | 0 | 0 | 0 | 0.013 | 0 | 0 | 0 | 0 | 0 | 0 |
| Au | 0 | 0 | 0 | 0 | 0 | 0 | 0 | 0 | 0 | 0 |
| Cu | 0 | 0.089 | 0.074 | 0 | 0 | 0 | 0.17 | 0.105 | 0 | 0.032 |
| Pb | 0 | 0.564 | 0 | 0 | 0 | 0 | 0.611 | 0.523 | 0 | 0.551 |
| Se | 0 | 0 | 0.012 | 0.008 | 0.014 | 0.015 | 0.011 | 0.02 | 0.055 | 0.028 |
| As | 0 | 0.023 | 0.066 | 0.046 | 0.036 | 0.021 | 0.029 | 0.035 | 0.043 | 0.051 |
| Sum | 99.637 | 99.505 | 99.134 | 98.59 | 98.857 | 98.62 | 97.861 | 99.199 | 99.722 | 98.385 |

values of the olivine band in the Raman spectra of ordinary chondrites from 10 $cm^{-1}$ for weakly shocked to 21 $cm^{-1}$ for strongly shocked meteorites. The calculated FWHM values of ~14–17 $cm^{-1}$ in the Mahadevpur meteorite are in accordance with the shock stage of S4 as determined from petrographical studies. The S4 shock-grade classification of the Mahadevpur meteorite corresponded to relatively medium shock pressure of 30–35 GPa (ref. 34). Recently, Mazumder *et al.*[35] have reported modification of the shock stage of the Mahadevpur sample from S1 to S4–S5, which is consistent with our observations.

The Raman spectra of the Mahadevpur sample displayed different carbon phases between 1000 and 2000 $cm^{-1}$ (Figure 6). In general, the Raman spectra of nanodiamonds exhibit two broad bands, corresponding to the $F_{2g}$ and $E_{2g}$ modes, with centres at 1326 and 1590 $cm^{-1}$ respectively. However, it has been reported that diamonds are only found in trace amounts in meteorites and micrometeorites as nanoparticles[36]. The sharp peak centred at 1333 $cm^{-1}$ is characteristic of the first-order Raman band ($F_{2g}$) of diamond representing the main C–C bond vibration in diamond (carbon sp3 bonding), and the broad bands centred at ~1358 and 1600 $cm^{-1}$ are the D- and G-bands respectively, of amorphous carbon[9,37]. The Raman band ($E_{2g}$) at 1600 $cm^{-1}$ has been attributed to carbon sp2 bonding graphitic structures[38]. However, the spectra of chemical vapour deposition (CVD) of nanodiamonds typically exhibit weak and broad features at 1152 and 1454 $cm^{-1}$, which have been utilized as markers for the presence of nanodiamonds[39–41]. Another peak at 1270 $cm^{-1}$ arising due to $2A_{1g}$ modes of vibration was also associated with nanodiamonds[42,43]. The broad characteristics at 1800 and ~1920 $cm^{-1}$ could be due to combinations or overtones. Strong background fluorescence is indicated by the relatively low peak intensities of these bands. This could be a result of the amorphous nature of the sample or its tiny grain size.

Raman characteristic D and G band peak positions and intensities vary according to the degree of ordering in the carbonaceous material[9,44]. In order to minimize background fluorescence, the least-squares moving average trend was used to find the best fit of the Raman spectra for the FWHM calculation, and authentication of the result can be found from different shock metamorphic environments[44–46]. FWHM values vary depending on the method of diamond synthesis, with 2–3 $cm^{-1}$ being typical for static

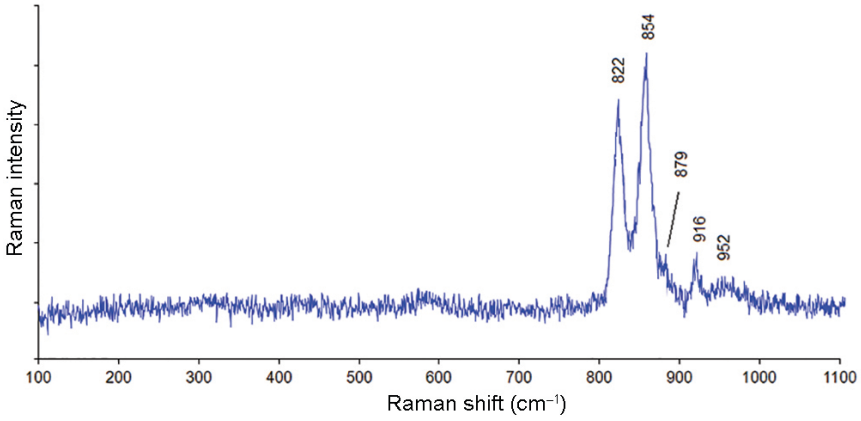


**Figure 4.** Characteristic olivine doublet observed at 822 and 854 $cm^{-1}$ for the Mahadevpur H4/5 chondrite in the Raman spectra. Ringwoodite signal is observed at 879 $cm^{-1}$.

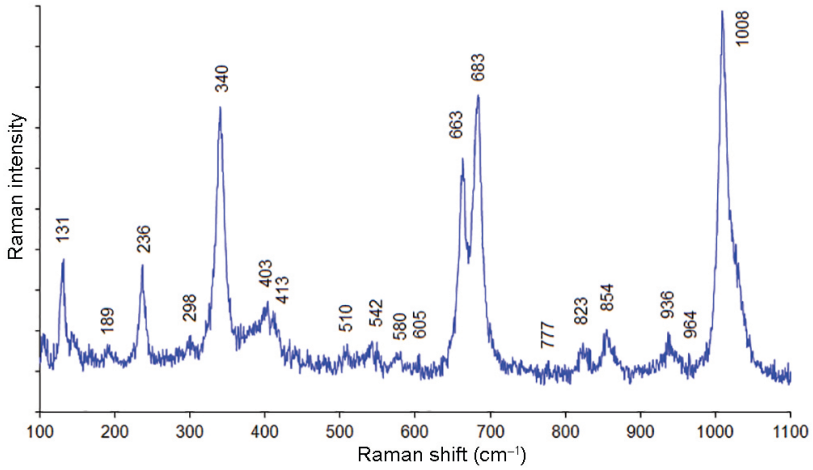


**Figure 5.** Raman spectrum of the Mahadevpur H4/5 chondrite exhibiting pyroxene.

high-pressure diamonds, 3–25 $cm^{-1}$ indicating CVD diamonds, and 10–120 $cm^{-1}$ being characteristic of shock-induced diamonds[47]. The calculated FWHM value for the D peak, which is ~67 $cm^{-1}$, falls within the typical range 10–120 $cm^{-1}$ for diamonds induced by shock[47], indicating the type of shock metamorphism present in the meteorite sample. The degree of ordering is indicated by the relative intensities of the ~1358 $cm^{-1}$ ($I_D$) and 1600 $cm^{-1}$ ($I_G$) peaks and their peak width, which is expressed as FWHM. The Raman intensity ratio of the diamond ($I_D$) and graphite ($I_G$) peaks was attributed to graphitic carbon by Wopenka *et al.*[48], with the range being fairly well ordered graphite ($I_D/I_G < 0.5$), disordered graphite ($0.51 < I_D/I_G < 1.1$) and glassy carbon ($I_D/I_G > 1.1$). The calculated $I_D/I_G$ ratio ~1.07 in the Mahadevpur sample indicates the presence of disordered graphite. Diamond is a typical high-pressure phase, and shock transformation from graphitic material has been proposed as one of the processes for its origin[22]. Primitive meteorites contain nanodiamonds with an abundance of ~1500 parts per million by weight and a mean size of ~2.6 nm (refs 22, 23). To estimate the size of nanodiamonds from the Raman spectra, we considered the FWHM value of the 1333 $cm^{-1}$ diamond peak as ~2.88 $cm^{-1}$ (ref. 49), which suggest a particle size of <50 nm. However, all other peaks and features associated with nanodiamonds are visible; some spectra lacked the Raman diamond peak at 1333 $cm^{-1}$ (Figure 6 *b*). The presence of nanodiamond phases is further confirmed by powder XRD pattern (Figure 7). In this case, the XRD pattern has been used as a supplementary tool for the identification of diamonds. The other mineral phases observed in the XRD pattern include olivine, plagioclase, enstatite and kamacite.

## Conclusion

Here we present EPMA, Raman spectroscopic analysis and powder XRD data on the Mahdevpur ordinary chondrites. The observed Raman band positions and relative intensities are consistent with the chemical composition for olivines and pyroxenes. Three metallic phases, viz.

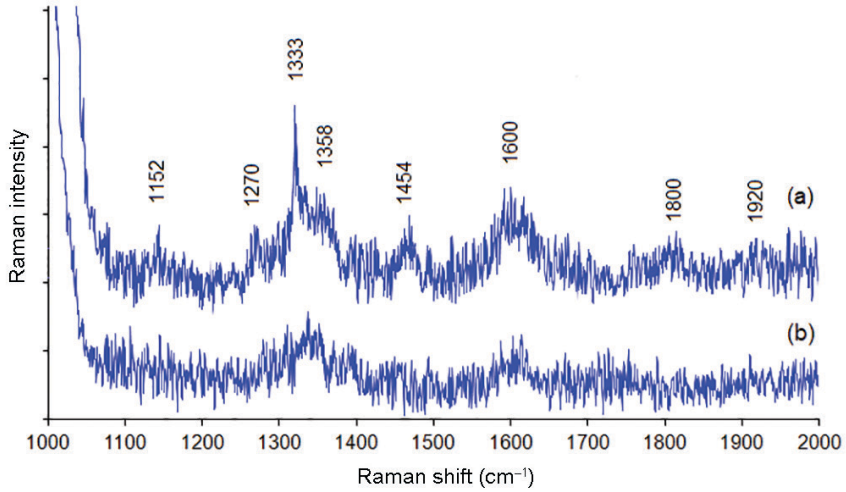


**Figure 6.** Raman spectra of the Mahadevpur H4/5 chondrite exhibiting different carbon phases.

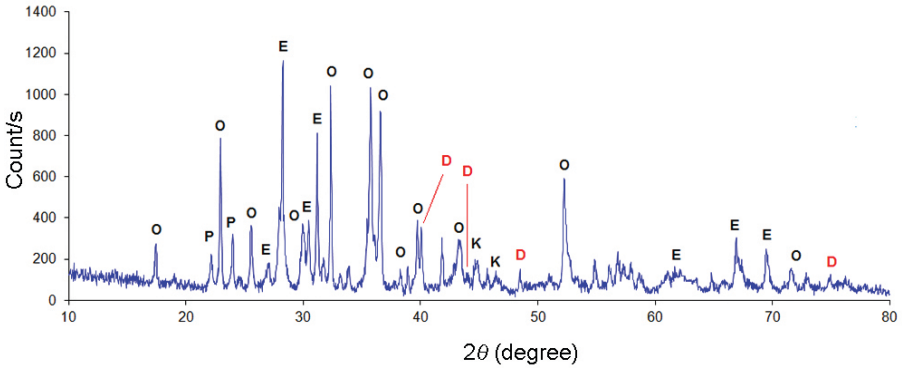


**Figure 7.** Powder X-ray diffraction pattern of the Mahadevpur H4/5 chondrite (O, Olivine; P, Plagioclase; E, Enstatite; D, Diamond; K, Kamacite).

kamacite (near pure end Fe)-taenite $\gamma$-(Fe, Ni) and tetrataenite (Fe–Ni) are identified in the meteorite. Several other phases like pure chromite, chlor-apatite, merrillite and plagioclase feldspar are also observed. The XRD pattern provided independent validation of the nanodiamonds. Diamond has a sharp Raman peak at 1333 $cm^{-1}$, while amorphous carbon has broad peaks at ~1358 and 1600 $cm^{-1}$, which are the D- and G-bands respectively. The FWHM value of the peak at 1333 $cm^{-1}$ was ~2.88 $cm^{-1}$, suggesting a nanodiamond particle sizes of <50 nm. The calculated $I_D/I_G$ ($I_D$ ~ 1358 $cm^{-1}$/$I_G$ ~ 1600 $cm^{-1}$) ratio of ~1.07 in the Mahadevpur chondrite implies the presence of disordered graphite.


1. Krot, A. N., Keil, K., Scott, E. R. D., Goodrich, C. A. and Weisberg, M. K., Classification of meteorites and their genetic relationships. In *Treatise on Geochemistry, 1.* (eds Turekian, K. K. and Holland, H. D.), Elsevier, Amsterdam, The Netherlands, 2013, 2nd edn, pp. 1–63.
2. Dhingra, D. *et al.*, Spectacular fall of the Kendrapara H5 chondrite. *Meteorit. Planet. Sci*., 2004, **39**(S8), A121–A132.
3. Parthasarathy, G. and Sarma, S. R., High-temperature electrical and thermal properties of Burdett, Dalhart, Faucet and Wellman ordinary chondrites. *Curr. Sci*., 2004, **86**(10), 1366–1368.
4. Bhandari, N. *et al.*, Bhawad, LL6 chondrite: chemistry, petrology, noble gases, nuclear tracks, and cosmogenic radionuclides. *Meteorit. Planet. Sci*., 2005, **40**(7), 1015–1021.
5. Bhandari, N. *et al.*, Ararki (L5) chondrite: the first meteorite find in Thar desert of India. *Meteorit. Planet. Sci*., 2008, **43**(4), 761–770.
6. Bhandari, N., Murty, S. V. S., Mahajan, R. R., Parthasarathy, G., Shukla, P. N., Sisodia, M. S. and Rai, V. K., Kaprada L(5/6) chondrite: chemistry, petrography, noble gases and nuclear tracks. *Planet. Space Sci.*, 2009, **57**(14–15), 2048–2052.
7. Chandra, U., Parthasarathy, G., Shekar, N. V. C. and Shau, P., X-ray diffraction, Mössbauer spectroscopic and electrical resistivity studies on Lohawat meteorite under high-pressure up to 9 GPa. *Chem. Erde*, 2013, **73**, 197–203.
8. Agwaral, V., Parthasarathy, G., Sisodia, M. S. and Bhandari, N., Fall, mineralogy and chemistry of Nathdwara H6 chondrite. *Geosci. Front*., 2014, **5**(3), 413–417.
9. Saikia, B. J., Parthasarathy, G. and Borah, R. R., Nanodiamonds and silicate minerals in ordinary chondrites as determined by micro-Raman spectroscopy. *Meteorit. Planet. Sci*., 2017, **52**(6), 1146–1154.
10. Saikia, B. J., Parthasarathy, G., Borah, R. R., Satyanarayanan, M., Borthakur, R. and Chetia, P., Spectroscopy and mineralogy of a fresh meteorite fall Kamargaon (L6) chondrite. *Proc. Indian Natl. Sci. Acad*., 2017, **83**(4), 941–948.
11. Saikia, B. J., Parthasarathy, G. and Borah, R. R., Mineralogy of meteorites from the North-eastern India: a brief review. *Geomaterials*, 2017, **7**(3), 83–95.

12. Saikia, B. J., Parthasarathy, G. and Borah, R. R., Raman and Infrared spectroscopic tentative identification of organic traces in Sadiya (LL5) ordinary chondrite. *Adv. Astrophys.*, 2018, **3**(4), 250–256.
13. Chandra, U., Pandey, K. K., Parthasarathy, G. and Sharma, M. S., High-pressure investigations on Piplia Kalaneucrite meteorite using *in situ* X-ray diffraction and $^{57}$Fe Mössbauer spectroscopic technique up to 16 GPa. *Geosci. Front*., 2016, **7**(2), 265–271.
14. Weisberg, M. K. *et al.*, The Meteoritical Bulletin No. 94. September 2008. *Meteorit. Planet. Sci*., 2008, **43**(9), 1551–1588.
15. Saikia, B. J., In *Ordinary Chondrites from North-East India: A Raman and Infrared Spectroscopic Approach*, Cambridge Scholar Publishing, UK, 2020, 1st edn, pp. 15–31.
16. Russell, S. S. *et al.*, The Meteoritical Bulletin No. 88, 2004 July. *Meteorit. Planet. Sci*., 2004, **39**(8), A215–A272.
17. Saikia, B. J., Parthasarathy, G. and Sarmah, N. C., Spectroscopic characterization of olivine [$(Fe,Mg)_2SiO_4$] in Mahadevpur H4/5 ordinary chondrite. *J. Am. Sci.*, 2009, **5**(4), 71–78.
18. Saikia, B. J. and Parthasarathy, G., Spectroscopic investigation of Mahadevpur H4/5 ordinary chondrite. *Geochim. Cosmochim. Acta*, 2009, **73**, 1144.
19. Saikia, B. J., Parthasarathy, G., Borah, R. R. and Borthakur, R., Raman spectroscopic study of Dergaon H5 and Mahadevpur H4/5 chondrite. In 47th Lunar and Planetary Science Conference, 2016, p. 1799.
20. Dehingia, N. and Baruah, G. D., Extended red emission in Mahadevpur (Namsai) meteorite. *Spectrosc. Lett.*, 2010, **43**, 144–147.
21. Murty, S. V. S. *et al.*, Jodia (L5) and Mahadevpur (H4/5): two recent ordinary chondrite falls in India. In 72nd Annual Meteoritical Society Meeting, Nancy, France, 2009, p. 5058.
22. Ott, U., Interstellar grains in meteorites. *Nature*, 1993, **364**, 25–33.
23. Ott, U., Nanodiamonds in meteorites: properties and astrophysical contex. *J. Achiev. Mater. Manuf. Eng.*, 2009, **37**(2), 779–784.
24. Jones, A. P. and d'Hendecourt, L. B., Interstellar nanodiamonds. In *Astrophysics of Dust* (eds Witt, A. N., Clayton, G. C. and Draine, B. T.), ASP Conference Series, Proceedings of the Conference held 26–30 May 2003, Estes Park, Colorado, 2004, vol. 309, p. 589.
25. Saikia, B. J., Parthasarathy, G., Borah, R. R., Borthakur, R. and Sarmah, A. J. D., Meteorite fall at Sadiya, India: a Raman spectroscopic classification. *J. Astrophys. Aerosp. Technol*., 2017, **5**(2), 1000149.
26. Saikia, B. J., Parthasarathy, G. and Borah, R. R., Silicates in Kamargaon (L6) chondrite: a Raman spectroscopic study. *Open Access J. Math. Theor. Phys.*, 2018, **1**(6), 225–230.
27. Yu, Y. G. and Wentzcovitch, R. M., Density functional study of vibrational and thermodynamic properties of ringwoodite. *J. Geophys. Res. Atmos.*, 2006, **111**, B12202.
28. Chopelas, A., Single crystal Raman spectra of forsterite, fayalite, and monticellite. *Am. Min.*, 1991, **76**, 1101–1109.
29. Fritz, J., Greshake, A. and Stöffler, D., Micro Raman spectroscopy of plagioclase and maskelynite in Martian meteorites: evidence of progressive shock metamorphism. *Antarct. Meteor. Res*., 2005, **18**, 96–116.
30. Hofmeister, A. M., Xu, J., Mao, H. K., Bell, P. M. and Hoering, T. C., Thermodynamics of Fe–Mg olivines at mantle pressures: mid and far-infrared spectroscopy at high pressure. *Am. Min.*, 1989, **74**, 281–306.
31. Chopelas, A., Thermal properties of forsterite at mantle pressures derived from vibrational spectroscopy. *Phys. Chem. Miner.*, 1990, **17**, 149–156.
32. Rull, F., Munoz-Espadas, M. J., Lunar, R. and Martinez-Frias, J., Raman spectroscopic study of four Spanish shocked ordinary chondrites: Canellas, Olmedilla de Alarcon, Reliegos and Olivenza. *Philos. Trans. R. Soc. A*, 2010, **368**, 3153–3166.
33. Miyamoto, M. and Ohsumi, K., Micro-Raman spectroscopy of olivines in L6 chondrites: evaluation of the degree of shock. *Geophys. Res. Lett.*, 1995, **22**, 437–440.
34. Stoffler, D., Keil, K. and Scott, E. R. D., Shock metamorphism of ordinary chondrites. *Geochim. Cosmochim. Acta*, 1991, **55**, 3845–3867.
35. Mazumdar, A. C., Pati, J. K., Singh, A. K., Bhagabaty, B., Phukan, S. and Borah, P., Petrography, mineral chemistry, metamorphism and Raman spectroscopic studies of Mahadevpur fall meteorite, India. *Geol. J*., 2023, **58**, 3630–3645.
36. Dai, Z. R., Bradley, J. P., Joswiak, D. J., Brownlee, D. E., Hill, H. G. M. and Genge, M. J., Possible *in situ* formation of meteoritic nanodiamonds in the early solar system. *Nature*, 2002, **418**, 157–159.
37. Knight, D. S. and White, W. B., Characterization of diamond films by Raman spectroscopy. *J. Mater. Res*., 1989, **4**, 385–393.
38. Nasdala, L., Smith, D. C., Kaindl, R. and Zieman, M. A., EMU Notes in Mineralogy-6. In *Spectroscopic Methods in Mineralogy* (eds Beran, A. and Libowitzky, E.), Eotvos University Press, Budapest, Hungary, 2004, pp. 281–343.
39. Zhou, D., Gruen, D. M., Qin, L. C., McCauley, T. G. and Krauss, A. R., Control of diamond film microstructure by Ar additions to $CH_4/H_2$ microwave plasmas. *J. Appl. Phys*., 1998, **84**, 1981–1989.
40. Ferrari, A. C. and Robertson, J., Origin of the 1150 cm$^{-1}$ Raman mode in nanocrystalline diamond. *Phys. Rev. B*, 2001, **63**, 121405(R).
41. Popov, C., Kulisch, W., Gibson, P. N., Ceccone, G. and Jelinek, M., Growth and characterization of nanocrystalline diamond/amorphous carbon composite films prepared by MWCVD. *Diam. Relat. Mater.*, 2004, **13**, 1371–1376.
42. Veres, M., Toth, S. and Koos, M., Grain boundary fine structure of ultrananocrystalline diamond thin films measured by Raman scattering. *Appl. Phys. Lett.*, 2007, **91**, 031913.
43. May, P. W., Smith, J. A. and Rosser, K. N., 785 nm Raman spectroscopy of CVD diamond films. *Diam. Relat. Mater.*, 2008, **17**, 199–203.
44. El Goresy, A., Gillet, P., Chen, M., Knstler, F., Graup, G. and Stahle, V., *In situ* discovery of shock-induced graphite–diamond phase transition in gneisses from the Ries Crater, Germany. *Am. Min.*, 2001, **86**, 611–621.
45. Mostefaoui, S., El Goresy, A., Hoppe, P., Gillet, P. and Ott, U., Mode of occurrence, textural settings and nitrogenisotopic compositions of *in situ* diamonds and other carbon phases in the Bencubbin meteorite. *Earth Planet. Sci. Lett*., 2002, **204**, 89–100.
46. Gucsik, A., Ott, O., Marosits, E., Karczemsk, A., Kozanecki, M. and Szurgot, M., Micro-Raman study of nanodiamonds from Allende meteorite. In *Organic Matter in Space, Proceedings of the International Astronomical Union, IAU Symposium*, 2008, vol. 251, pp. 335–340.
47. Miyamoto, M., Micro-Raman spectroscopy of diamonds in the Canyon Diablo iron meteorite: implication for the shock origin. *Antarct. Meteor. Res*., 1998, **11**, 171–177.
48. Wopenka, B., Xu, Y. C., Zinner, E. and Amari, S., Murchison presolar carbon grains of different density fractions: a Raman spectroscopic perspective. *Geochim. Cosmochim. Acta*, 2013, **106**, 463–489.
49. Yoshikawa, M., Mori, Y., Maegawa, M., Katagiri, G., Ishida, H. and Ishitani, A., Raman scattering from diamond particles. *Appl. Phys. Lett.*, 1993, **62**, 3114–3116.

ACKNOWLEDGEMENTS. We thank the three anonymous reviewers and Prof. Somnath Dasgupta (subject editor) for their in-depth suggestions that helped improve the manuscript. We also thank the Director, Indian Institute of Technology Guwahati for providing Raman and powder XRD facilities for characterization of the meteorite. N.V.C.R. thanks Science Engineering Research Board, New Delhi for a National research project (IR/S4/ESF-18/2011, dated 12.11.2013) which facilitated establishment of the EPMA laboratory, and BHU, Varanasi for awarding a faculty incentive grant through IOE scheme. G.P. thanks Indian National Science Academy (INSA), New Delhi, and National Institute of Advanced Studies, Bengaluru for support through the INSA Senior Scientist scheme.

Received 30 October 2023; re-revised accepted 19 January 2024

doi: 10.18520/cs/v126/i5/574-582